ORNL/SPR-2023/2960

Multiscale Modeling of Radiation Damage in UO_2 under Accelerated Burnup Conditions

Amani Cheniour
Ian Greenquist
Nathan A. Capps
Christian M. Petrie

July 2023

OAK RIDGE National Laboratory

ORNL IS MANAGED BY UT-BATTELLE LLC FOR THE US DEPARTMENT OF ENERGY

ORNL/SPR-2023/2960

Advanced Fuels Campaign Milestone Report

MULTISCALE MODELING OF RADIATION DAMAGE IN UO_2 UNDER ACCELERATED BURNUP CONDITIONS

Amani Cheniour
Ian Greenquist
Nathan A. Capps
Christian M. Petrie

July 2023

Prepared by
OAK RIDGE NATIONAL LABORATORY
Oak Ridge, TN 37831
managed by
UT-Battelle LLC
for the
US DEPARTMENT OF ENERGY
under contract DE-AC05-00OR22725

CONTENTS

LIST OF FIGURES

LIST OF TABLES

ABBREVIATIONS

CD	cluster dynamics
CNT	classical nucleation theory
HFIR	High Flux Isotope Reactor
LWR	light-water reactor
MOOSE	Multiphysics Object-Oriented Simulation Environment
ORNL	Oak Ridge National Laboratory
PIE	postirradiation examination
PKA	primary knocked-on atom

ACKNOWLEDGMENTS

This work was supported by the Advanced Fuels Campaign within the US Department of Energy (DOE) Office of Nuclear Energy (NE). This research made use of Idaho National Laboratory computing resources, which are supported by DOE NE and the Nuclear Science User Facilities under contract no. DE-AC07-05ID14517.

ABSTRACT

Accelerated fuel qualification (AFQ) is a methodology by which new nuclear fuels are developed in an accelerated time frame compared with historical fuel qualification approaches. AFQ generally relies on high-fidelity physics-based modeling and simulation tools to adequately describe fuel performance as well as on revolutionary methods to accelerate burnup accumulation and collect relevant data more quickly. This report summarizes the use of advanced fuel modeling and simulation tools to evaluate microstructures from commercially irradiated fuel and microstructures from proposed MiniFuel irradiations, in which burnup accumulation is accelerated while prototypic temperature conditions are maintained. In this milestone, we used the mesoscale fuel performance code MARMOT to model the evolution of irradiated UO_2 microstructures and their potential restructuring at high burnup. The simulation conditions were informed by BISON models of both commercially irradiated fuel and MiniFuel.

1. INTRODUCTION

The development and improvement of nuclear fuel concepts for safer and more efficient reactor operation is crucial because of the increasing demand and need for nuclear power in the United States. Along with the extensive postirradiation examination (PIE) efforts to evaluate fuel performance factors such as fission gas release, fuel swelling, and cracking, advanced modeling and simulation tools play a major role in understanding the underlying physics and mechanisms of fuel performance. Accelerated fuel qualification enables more rapid assessment of fuel performance and microstructural evolution with burnup. MiniFuel irradiations [1] at the High Flux Isotope Reactor (HFIR) in Oak Ridge National Laboratory have been performed recently to gather PIE data on UO_2 MiniFuel specimens.

Advanced nuclear fuel modeling and simulation tools such as BISON [2] and MARMOT [3] have been developed to evaluate fuel performance in light-water reactors (LWRs) under normal and accidental conditions. Fuel performance codes contain mechanistic models derived from verification with respect to analytical solutions and validation using experimental data. However, many models are purely empirical and rely on PIE data of fuels irradiated in various conditions, although the availability of these PIE data is limited. Modeling high-burnup fuel is of particular interest to the potential extension of the fuel burnup in LWRs beyond the current 62 GWd/mtU.

The fuel models available in the engineering-scale fuel performance code BISON can be highly sensitive to microstructural features such as fuel porosity and grain size [4]. Modeling the microstructural evolution of UO_2 has been the subject of much research [5, 6, 7, 8, 9, 10]. The phase field method is a powerful tool to predict a material's microstructural evolution [11] and has been applied to radiation damage problems [8, 12, 13, 6]. Supported by experimental or atomistic simulation data such as diffusion coefficients and formation energies, the phase field method provides helpful insight into the effects of radiation on nuclear fuel microstructures.

In our previous Advanced Fuels Campaign milestone M3FT-23OR020205042, we addressed the issue of modeling restructuring in the lower-temperature region of an LWR fuel pellet. By combining a MARMOT phase field radiation damage model that tracks UO_2 grain boundaries and fission gas bubbles and a nucleation algorithm, we developed a physics-based model to predict the onset of nucleation of smaller grains, thus simulating the restructuring reported in the literature [14, 15]. In continuation of this effort, the present work adds significant capabilities to our previous UO_2 microstructural evolution model by accounting for the clustering and re-solution of fission gas atoms [7] as well as the Monte Carlo simulation-based [16] production rates of point defects and their reaction terms. Additionally, we included a classical nucleation theory (CNT)–based model to evaluate the probability of intergranular fission gas bubble nucleation in the microstructure. These additional layers of complexity significantly improve the model's physics and enable the simulation of UO_2 microstructures from the initial condition of the UO_2 up to high burnup.

Section 2. presents a 2D multiscale approach used to couple the phase field code MARMOT with the cluster dynamics (CD) code Xolotl and the binary collision Monte Carlo code Magpie. Xolotl is used to model the fission gas behavior in UO_2 [7], whereas Magpie simulates the production of U vacancies and interstitials under a given fission rate [17, 16]. Section 3. explains the simulation setup. Section 4. presents and discusses the results of the multiscale model applied at a high fission rate to simulate the effects of accelerated burnup on UO_2 microstructural evolution.

2. METHODS

2.1 PHASE FIELD

The mesoscale fuel performance code MARMOT uses the phase field method and is based on the finite element Multiphysics Object-Oriented Simulation Environment (MOOSE) [18]. This work used the grand-potential formulation of the phase field model described by Aagesen et al. [19]. The grand-potential density is obtained through a Legendre transform of the Gibbs free-energy density [20]. The Allen–Cahn equation was used to model fission gas bubbles and grains such that

$$\frac{\partial \eta_i}{\partial t} = -L_i \frac{\delta \Omega}{\delta \eta_i}, \tag{1}$$

where i represents either the bubble phase or a grain; η_i is the corresponding order parameter or phase field such that $\eta_i = 1$ inside the bubble or grain, $\eta_i = 0$ outside the bubble or grain, and $0 < \eta_i < 1$ at interfaces; t is time; L_i is the phase mobility; and Ω is the grand-potential function. In this work, $i = 0$ refers to the bubble phase, whereas $i \in \{1, 2, ..., N\}$ refers to a grain. The grand-potential function is the sum of various contributions such that for N grains and a bubble phase,

$$\Omega = \int_V (m f_B + \sum_{i=0}^{N} \frac{\kappa_i}{2} |\nabla \eta_i|^2 + h_m \omega_m + h_b \omega_b)\, dV, \tag{2}$$

where m is a constant weight; f_B is the bulk free energy; κ_i is the gradient energy coefficients for phase i; h_m and h_b are the switching functions for UO_2 and bubbles, respectively; and ω_m and ω_b are the corresponding grand-potential densities. The bulk free energy is expressed as

$$f_B = \sum_{i=0}^{N} (\frac{\eta_i^4}{4} - \frac{\eta_i^2}{2}) + \sum_{i=0}^{N} \sum_{j \neq i}^{N} \frac{\gamma_{ij}}{2} \eta_i^2 \eta_j^2 + \frac{1}{4}, \tag{3}$$

where γ_{ij} is a constant that allows for controlling the interfacial energy between grain boundaries and surface energies. The grand-potential functions are given by

$$\omega_m = f_m + f_d - \mu_g \rho_g - \mu_v \rho_v - \mu_{in} \rho_{in}, \tag{4}$$

and

$$\omega_b = f_b - \mu_g \rho_g - \mu_v \rho_v - \mu_{in} \rho_{in}, \tag{5}$$

where f_m is the free energy in the matrix, f_d is the free energy due to dislocations, and f_b is the free energy in the bubbles; g represents gas atoms, v represents U vacancy, and in represents U interstitial; μ_g, μ_v, and μ_{in} are the chemical potentials of the gas atoms, U vacancy, and U interstitial, respectively, such that for phase i, $\mu_i = \frac{\partial f_i}{\partial \rho_i}$; and ρ_g, ρ_v, and ρ_{in} are the atomic densities of the gas atoms, U vacancy, and U interstitial, respectively. For simplicity, the elastic energy was not modeled in this work. The switching functions h_m and h_b in Eq. (2) are given by

$$h_m = \frac{\sum_{i=1}^{N} \eta_i^2}{\sum_{i=0}^{N} \eta_i^2}, \tag{6}$$

and

$$h_v = \frac{\eta_0^2}{\sum_{i=0}^{N} \eta_i^2}, \tag{7}$$

The free-energy density f_m represents an ideal solution model, and f_b uses the Van der Waals gas Helmholtz free energy [6]. The ideal solution model and the Van der Waals gas Helmholtz free energy were both approximated by parabolic functions, similarly to the work done by Aagensen et al. [6]. Parabolic energy density approximation significantly improves the numerical convergence to the solution because it is continuously differentiable and allows small numerical errors in the solution without significantly affecting the convergence. The ideal solution free energy is given by

$$f_{ideal} = \frac{1}{V_a}\sum_j [E_{f_j} c_j + k_B T(c_j ln(c_j) + (1 - c_j) ln(1 - c_j))], \tag{8}$$

where E_{f_j} is the formation or incorporation energy, and k_B is Boltzmann's constant. Based on f_{ideal}, the parabolic matrix free-energy density f_m is given by

$$f_m = \frac{1}{2}[A_{m,g}(c_g - c_{g_{m,eq}})^2] + \frac{1}{2}[A_{m,v}(c_v - c_{v_{m,eq}})^2] + \frac{1}{2}[A_{m,in}(c_{in} - c_{in_{m,eq}})^2], \tag{9}$$

where $A_{i,j}$ are parabolic coefficients, c_j are concentration variables of species j, and $c_{j_{i,eq}}$ are equilibrium concentrations in phase i. The ideal solution model used in this work also follows the approach of Aagesen et al. [6], which assumes that gas atoms and U vacancies do not occupy the same lattice site. This approach was chosen because the current grand-potential formulation does not allow for obtaining a Legendre transform analytically for a multicomponent system on a single lattice. However, for site-conservation purposes, the equation should be modified in future work to account for potential gas atoms on U lattice sites by integrating a numerical solution of the corresponding grand-potential function.

The Van der Waals gas Helmholtz energy given in [6] is expressed as

$$f_{VdW} = n_g k_B T[ln(\frac{1}{n_Q(\frac{1}{n_g} - b)}) - 1] + f_0, \tag{10}$$

where n_g is the number density of fission gas atoms, n_Q is the quantum concentration, and f_0 is the difference between the ideal solution energy minimum and the Van der Waals gas energy minimum. The parabolic fit of the Van der Waals gas Helmholtz energy density equation, f_b, also followed the approach of Aagesen et al. [6]:

$$f_b = \frac{1}{2}[A_{b,g}(c_g - c_{g_{b,eq}})^2] + \frac{1}{2}[A_{b,v}(c_v - c_{v_{b,eq}})^2] + \frac{1}{2}[A_{b,in}(c_{in} - c_{in_{b,eq}})^2], \tag{11}$$

The $A_{b,j}$ coefficients and the equilibrium concentrations $c_{j_{eq}}$ were determined for each temperature considered in this study such that $c_{b_{eq}}$ is the gas concentration at the minimum of the Van der Waals gas Helmhotlz energy [6] and $c_{v_{eq}} = 1 - c_{b_{eq}}$. For both gas and vacancy, $A_{b,j}$ was set to the same value. The fitting parameters are given in Table 1.

Table 1. Parabolic free energies parameters

Parameter	800°C	950°C
$A_{m,g}$ (eV/nm^3)	10,151	9,969
$A_{b,g}$ (eV/nm^3)	501	601
$A_{m,v}$ (eV/nm^3)	8,388	8,196.9
$A_{b,v}$ (eV/nm^3)	501	601
$A_{m,in}$ (eV/nm^3)	20,647	20,416
$A_{b,in}$ (eV/nm^3)	501	601
$c_{g_{m,eq}}$	$\exp(-\frac{E_{fg}}{k_B T})$	$\exp(-\frac{E_{fg}}{k_B T})$
$c_{v_{m,eq}}$	$\exp(-\frac{E_{fv}}{k_B T})$	$\exp(-\frac{E_{fv}}{k_B T})$
$c_{in_{m,eq}}$	$\exp(-\frac{E_{fin}}{k_B T})$	$\exp(-\frac{E_{fin}}{k_B T})$
$c_{g_{b,eq}}$	0.442	0.443
$c_{v_{b,eq}}$	0.558	0.557
$c_{in_{b,eq}}$	0	0

The dislocation free-energy density was modeled using the equation

$$f_{disloc} = \frac{1}{2} G b^2 \rho_d, \tag{12}$$

where G is the UO_2 shear modulus, b is the length of the Burgers vector, and ρ_d is the dislocation density. Similar to the high-burnup structure formation model in Abdoelatef et al. [9], the empirical relationship between dislocation density ρ_d (m/m^3) and burnup β (MWd/kgU) was used:

$$log(\rho_d) = 2.2 \times 10^{-2} \beta + 13.8, \tag{13}$$

which was obtained from dislocation density measurements in the peripheral region of a fuel pellet irradiated in a boiling-water reactor [15]. This expression was used in this study as a substitute for dislocation density calculations based on defect accumulation, which typically use rate theory [21, 22]. The dislocation density was assumed to be uniform everywhere in the domain outside of bubbles and nucleated grains, where it was set to zero.

In addition to grains and bubbles, the evolution of fission gas atoms was modeled by solving for their chemical potentials [20]:

$$\frac{\partial \mu_g}{\partial t} = \frac{1}{\chi_g} [\nabla \cdot (D_g \chi_g \nabla \mu_g) - \sum_{i=0}^{N} \frac{\partial \rho_g}{\partial \eta_i} \frac{\partial \eta_i}{\partial t} + \dot{G}_g], \tag{14}$$

The evolutions of U vacancies and U interstitials are given by:

$$\frac{\partial \mu_j}{\partial t} = \frac{1}{\chi_j} [\nabla \cdot (D_j \chi_j \nabla \mu_j) - \sum_{i=0}^{N} \frac{\partial \rho_j}{\partial \eta_i} \frac{\partial \eta_i}{\partial t} + \dot{G}_j + \dot{R}_j + \dot{S}_j], \tag{15}$$

where χ_j is the susceptibility, D_j is the diffusion coefficient, $\dot{G}_j$ is the production rate, $\dot{R}_j$ is the recombination between vacancies and interstitials, and $\dot{S}_j$ is the dislocation sink term. The atomic diffusion coefficients were multiplied by 10 at interfaces to obtain faster diffusion at grain boundaries and interfaces between bubbles and grains. The fission gas was assumed to be Xe only; therefore, its diffusivity followed

the expression by Turnbull [23]. The U vacancy and U interstitial diffusion coefficients were taken from Matzke [24].

The recombination term is given by

$$\dot{R}_j = \frac{V_a D_{in}}{a^2} \rho_{in} \rho_v, \tag{16}$$

The dislocation sink term follows:

$$\dot{S}_j = D_j \rho_d \rho_j, \tag{17}$$

The susceptibility for species j is given by

$$\chi_j = \frac{h_m}{A_{m,j} V_a^2} + \frac{h_b}{A_{b,j} V_a^2}, \tag{18}$$

where V_a is the atomic volume.

2.1.1 Model Parameters

Phase field model parameters are typically derived from physical quantities such as the grain boundary energy and mobility for the phase mobility L_i of grain i. For the bubble phase η_b, the phase mobility was chosen to allow a reasonable time step while still limiting the interface mobility by diffusion, as done in Aagensen et al. [6]. The grain phase mobility is expressed as

$$L_i = \frac{4}{3} \frac{M_{gb}}{l_{int}}, \tag{19}$$

where M_{gb} is the temperature-dependent grain boundary mobility, and l_{int} is the interfacial width. The gradient energy coefficient κ_i is expressed as

$$\kappa_i = \frac{3}{4} \sigma_i l_{int}, \tag{20}$$

where σ_i can, for instance, be the grain boundary energy or a surface energy depending on the interface's nature. For the bubble–UO_2 interface, this study considered that the interfacial energy was equal to the UO_2 surface energy, which is approximately two times higher than the UO_2 grain boundary energy [25]. The constant m is derived as

$$m = 6 \frac{\sigma_i}{l_{int}}, \tag{21}$$

2.1.2 Nucleation

This model used the phase field module of the MOOSE framework, which is used by MARMOT. The Grain Tracker algorithm [26] was used to reduce the computational cost by associating an order parameter with potentially more than a single grain when the number of grains exceeded the number of order parameters. This algorithm is particularly useful in recrystallization problems, in which the number of grains can rapidly increase, and does not require additional order parameters. This drastically reduces the number of degrees of freedom in the simulation.

The discrete nucleation algorithm available in MOOSE was used to generate new circular grains based on a provided nucleation probability through direct modification of a reserved-order parameter. Nucleation was

assumed to occur at a specified rate, which is a function of the nucleation driving force and temperature. The driving force Δf is a result of the dislocation energy, the energy caused by gas atoms and U vacancy accumulation in the matrix, and the interfacial energy. The CNT was used to compute the critical nucleation free energy G^* [27],

$$\Delta G^* = \frac{\pi \gamma^2}{\Delta f}, \tag{22}$$

where γ is the free energy of the interface, expressed as

$$\gamma = \frac{\sqrt{\kappa_i \mu}}{3\sqrt{2}}, \tag{23}$$

The CNT also provided the critical radius r^*, where the derivative of the free energy of a circular particle with respect to the radius is equal to zero. However, because r^* can be very small, a new nucleus can require a very refined mesh at the nucleation site. To mitigate this issue, a radius was set to be large enough to permit a reasonable mesh refinement level and, thus, a significantly lower computational cost. This is a limitation of the nucleation approach used in this work.

The nucleation rate J was calculated as

$$J = K \exp\left(-\frac{\Delta G^*}{k_B T}\right), \tag{24}$$

where K is the rate constant. A similar Arrhenius equation was used by Takaki et al. [28] in their nucleation rate model. The rate constant K was set to a value that limited the nucleated grains to a reasonable number every time step to avoid significant overlapping between preexisting nuclei and new nuclei, which is not prohibited in MOOSE's discrete nucleation algorithm. This nucleation rate calculation was performed on a trial-and-error basis. Additionally, to prevent overlaps, we computed the radial average of the value associated with new grains such that if a new grain or a bubble was within a given radius (set equal to the bubble radius), then the nucleation probability was zero. Everywhere else, the nucleation probability P was taken as [27]

$$P(t) = 1 - \exp(-J\Delta t), \tag{25}$$

Note that overlaps between new nuclei generated at the same time step are still possible. To address this issue, the maximum value that P could take was 10^{-5}; this avoided a large number of new nuclei at a single time step. Finally, within nucleated grains, the dislocation density was set to zero. This condition is a natural assumption in a recrystallization problem.

2.2 CLUSTER DYNAMICS

The finite difference CD code Xolotl [29, 30] is used to simulate fission gas clusters, assuming that all fission gas atoms are Xe [7]. Xolotl was coupled with MARMOT in the work by Kim et al. [7] through a recently developed coupling interface. Kim et al. [7] fully describes the coupled model; to avoid duplication of this effort, we provide only a brief summary here. The evolution of a cluster C_n is given as

$$\frac{\partial C_n}{\partial t} = y_n \dot{F} + D_n \nabla^2 C_n - Q(C_n), \tag{26}$$

where y_n is the fission yield of n Xe atoms, $\dot{F}$ is the fission rate density, D_n is the diffusion coefficient of cluster n, and $Q(C_n)$ is a reaction term. Reactions such as self-clustering, Xe atom emission, and Xe atom

re-solution are accounted for in $Q(C_n)$. All CD model parameters are given in Kim et al. [7]. In this work, both re-solution and self-clustering were included.

The coupling of MARMOT with Xolotl is an efficient approach to account for intragranular and intergranular fission gas behavior. In fact, modeling small Xe clusters or bubbles using a stand-alone MARMOT microstructural model would be highly inefficient because the level of mesh refinement necessary to capture such small features in the simulated domain would be significant. This is practically unfeasible because of the associated memory requirement. Instead, retrieving the Xe concentration from the CD calculations applied to the same simulation domain significantly cuts the computational cost. The idea is to evaluate the single-atom concentration at each finite element node based on the given cluster reaction rates and diffusion coefficients and pass it to MARMOT through the coupling interface. Xolotl also accounts for the presence of grain boundary and fission gas atoms by forcing the gas atom concentration to 0.0 at any point or node that belongs to these areas. Overall, this approach avoids explicitly modeling small intragranular bubbles in the finite element simulation. Xolotl passes only the Xe atom arrival rate at grain boundaries to MARMOT.

2.3 BINARY COLLISION MONTE CARLO

The binary collision Monte Carlo code Magpie is another MOOSE-based application and is designed to model collision cascades generated under neutron or ion irradiation. Magpie determines primary knocked-on atoms (PKAs) based on a given fission rate density and the elemental densities within a given material. Schwen et al. [16] details the use of Magpie and its coupling to a phase field model to predict the production rate of point defects. Magpie can track interstitial atoms, vacancies, and substitutional atoms. It first determines the PKA distribution across the mesh, based on the atomic number and mass of each element comprising the material in the finite element domain. Here, we chose a Magpie PKA generator that takes the UO_2 density at a specific time step to sample an empirical mass and energy distribution of fission fragments based on the work by Faust [31]. Once the number of PKAs is determined, the code performs collisions cascades resulting in the formation of point defects. Instantaneous recombination between vacancies and interstitials happens within damage cascades where thermal spikes occur. This is activated in Magpie if the distance between the annihilating point defects is within a given radius. In this work, we set this radius to the UO_2 lattice parameter 5.435 Å. Magpie's algorithms are fully detailed in Schwen, Schunert, and Jokisaar [16] and have been successfully applied [17, 16].

3. SIMULATION SETUP

All simulations were performed in 2D with a domain size of 15×15 μm. The basic mesh was set to 125×125 first-order quadrilateral elements, and three levels of mesh refinement were added at the initialization of the domain at interfaces only, such that the smallest element size was 60 nm. Mesh adaptivity was used throughout the simulation run on all order parameters and any new nuclei. The number of grains was four. An additional reserved-order parameter was used to include new nuclei before remapping them between the grain order parameters, which was enabled through Grain Tracker. The interfacial width l_{int} was set to 220 nm. Periodic boundary conditions were used in all the simulations.

The radius of a new nuclei is set to 675 nm, which is larger than the size of typical submicrometer grains in high-burnup structures reported in the literature [15, 14]. However, this choice was necessary to reduce the memory usage because each new nucleus induces further mesh refinement, which increases the number of degrees of freedom in the simulation. Similarly, the radius of a new bubble was set to 500 nm. The initial time step was set to 10^4 s, and the following time steps were allowed to increase to 5×10^4 s. All simulation parameters used in this work are shown in Table 2. For simplicity, temperatures and fission rates were assumed to remain constant throughout the simulation. Two temperatures were considered in this study: 800°C and 950°C. The initial domain did not contain intergranular fission gas bubbles.

Table 2. Simulation parameters

Parameter	Value	Reference
Initial grain number	4	—
Fission rate density $\dot{F}$ (fissions/nm^3/s)	1.16×10^{-7}	—
Nucleated initial grain radius (nm)	675	—
U density N_U (atoms/cm^3)	2.325×10^{22}	—
Nucleation rate constant K (/s)	10^{12}	—
U vacancy formation energy E_{f_v} (eV)	3.3	[32]
U interstitial formation energy $E_{f_{in}}$ (eV)	7.3	[32]
Xe incorporation energy E_{f_g} (eV)	3.88	[33]
U atomic volume V_a (nm^3)	0.04092	[34]
GB mobility activation energy Q (eV)	2.77	[35]
GB mobility rate constant M_0 (nm^2/eV/s)	1.4759×10^9	[35]
UO_2 shear stress G (GPa)	73	[15]
UO_2 Burgers vector length (nm)	0.39	[15]
Grain boundary energy σ_{gb} (J/m^2)	1.4125	[36]
Interfacial width l_{int} (nm)	220	—
U vacancy diffusion coefficient D_v (nm^2/s)	$2 \times 10^{11} \exp(-2.4/k_B/T)$	[24]
U vacancy diffusion coefficient D_{in} (nm^2/s)	$1 \times 10^{13} \exp(-2/k_B/T)$	[24]
Xe diffusion coefficient D_g (nm^2/s)	$7.6 \times 10^{-10} \exp(-35,250/T)$ $+1.14 \times 10^{-25} \sqrt{\dot{F}} \exp(-13,700/T)$ $+2 \times 10^{-40} \dot{F} \times 10^{18}$	[23]

The fission rate density $\dot{F}$ also varied depending on the considered case. The burnup β was calculated as

$$\beta(t) = 950 \frac{\dot{F}}{N_U} t, \tag{27}$$

where N_U is the U density in UO_2. Given the abundant production of point defects at the high fission rate density considered in this work, Magpie can rapidly require significant memory. To address this challenge, we isolated the Magpie simulation in a smaller 1.5×1.5 μm domain. Magpie computed the U vacancy and U interstitial production rates and passed them to the MARMOT simulation at each time step. The full coupling scheme is shown in Figure 1.

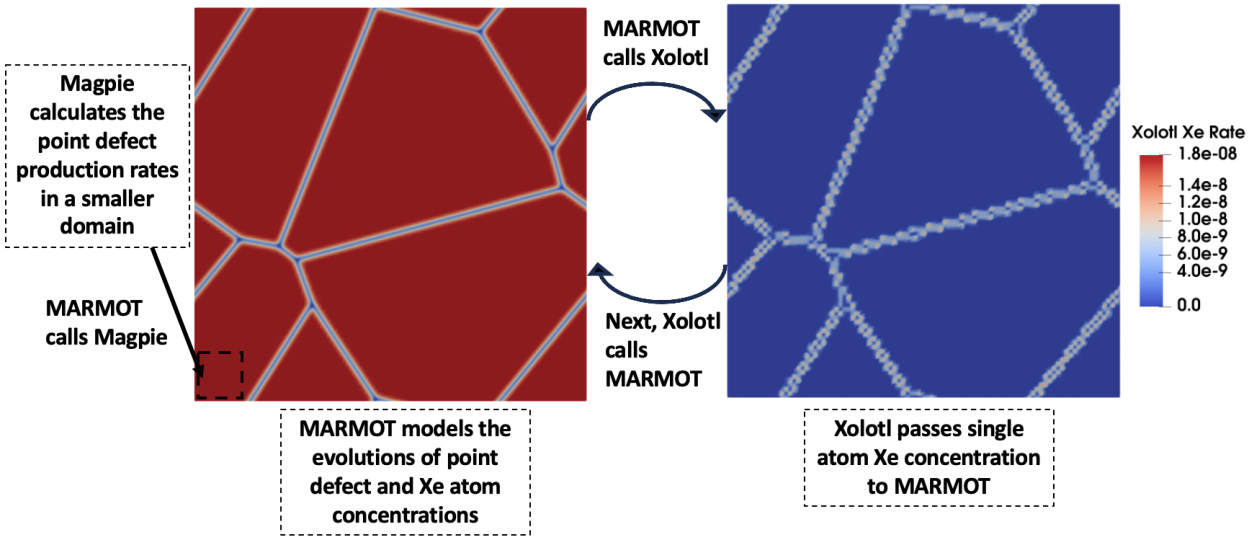

Figure 1. Magpie–MARMOT–Xolotl coupling scheme.

Similar to the work by Kim et al. [7], the Xolotl domain contained 126 × 126 nodes and was called by the coupling interface. The interface passed the locations of grain boundaries and bubbles to Xolotl, which in turn computed the concentrations of Xe clusters and single Xe atoms. The latter was then passed to MARMOT. Then, a new time step began. Magpie was called at the beginning of each time step. The coupling interface between Xolotl and MARMOT was updated to be compatible with the latest MOOSE release.

The present work simultaneously coupled MARMOT, Magpie, and Xolotl, which to our knowledge has not been done in previous work. The purpose of this approach is to lower the uncertainty related to the evolution of point defects and fission gas atoms and to improve our quantitative assessment of UO_2 microstructural features at high fission rates.

4. RESULTS AND DISCUSSION

To analyze the effect of temperature on the simulated defect concentration up to a final burnup of 23 MWd/kgU, the evolution of the average c_g, c_v, and c_{in} with burnup is plotted in Figure 2. The results show that at the same temperature, the U vacancy and U interstitial concentrations were significantly different. This is explained by the high diffusion coefficient of U interstitials, which leads to more absorption at sinks. The recombination rate was the same for both point defects. For lower burnups, the U vacancy concentration at 800°C was higher than the U vacancy concentration at 950°C; however, the U vacancy growth rate was higher at 950°C. This is also because more interstitials are absorbed at sinks at higher temperatures, which reduces the recombination with vacancies. The interstitial concentration evolution with temperature shows this effect. These results were expected given the kinetics of the problem.

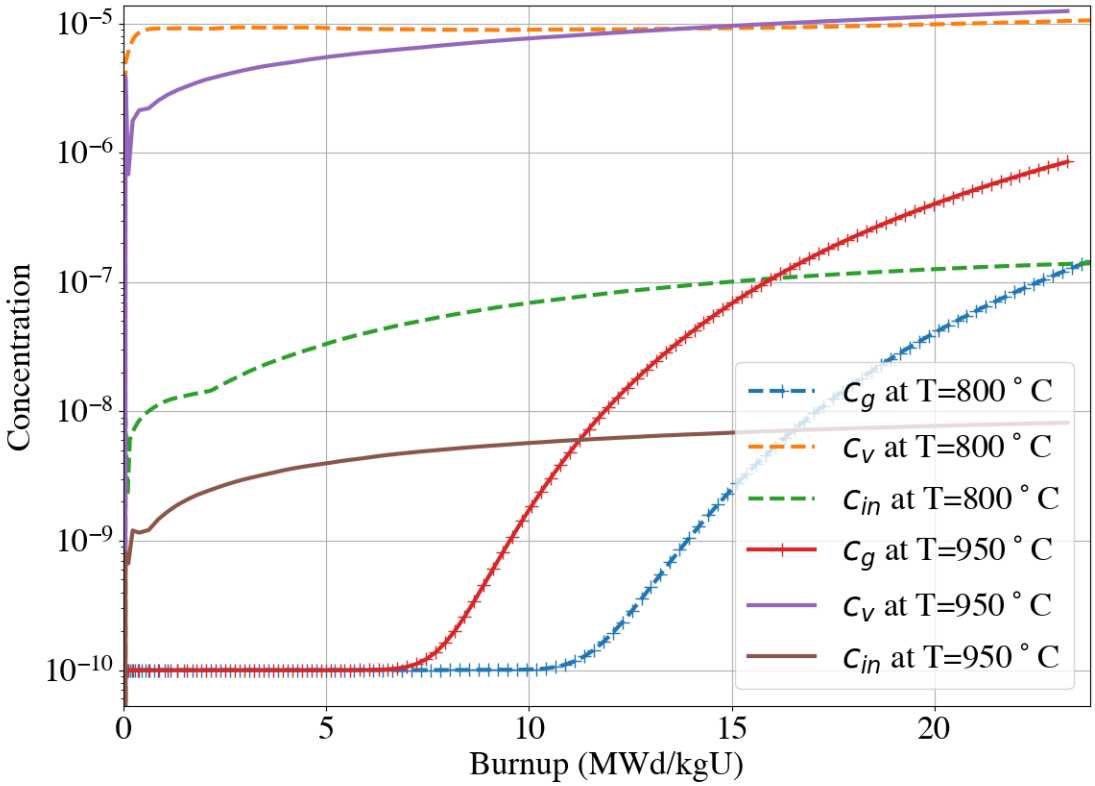

Figure 2. Evolution of the average U vacancy (c_v), U interstitial (c_{in}), and Xe atom concentrations (c_g) (logarithmic axis) with burnup (MWd/kgU).

Next, the evolution of the gas concentration obtained from Xolotl shows that the higher temperature caused an increase in the single Xe atom concentration. This was observed by Kim et al. [7] when comparing the simulation results at 1,000 and 1,800 K. The distribution of single Xe atoms is shown in greater detail in Figure 3, which shows c_g values across the simulation domain at both temperatures. Note that the scales

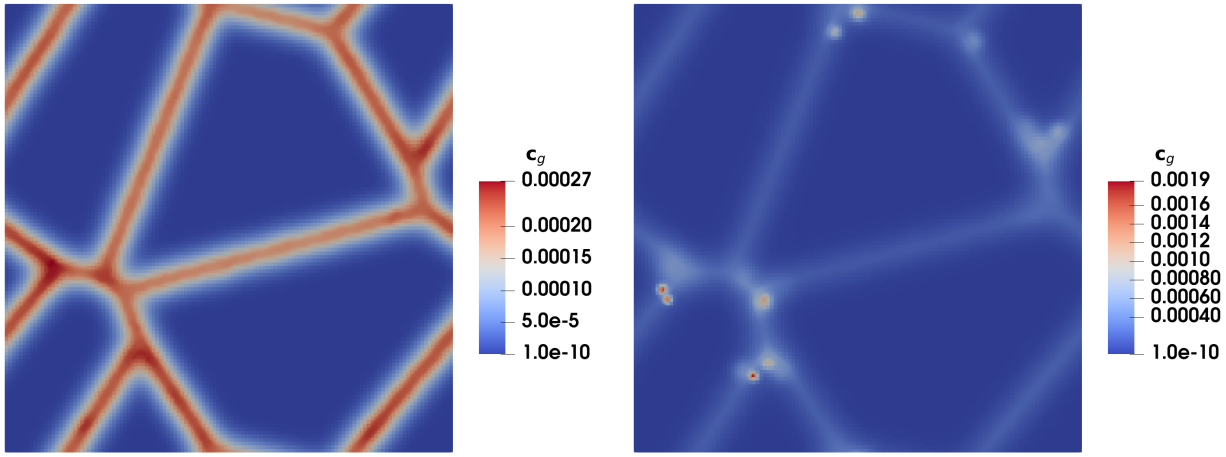

(a) T = 800°C. **(b) T = 950°C.**

Figure 3. Single Xe atom concentrations at a burnup of 23 MWd/kgU at (a) T = 800°C and (b) T = 950°C.

are different in each temperature case. The maximum c_g was almost an order of magnitude higher at 950°C than at 800°C. In fact, higher temperature drives more single-atom diffusion, which reduces the number of small intragranular bubbles [7]. Note that in Figure 3b, the highest Xe concentrations were obtained at or in the vicinity of triple junctions. Figure 3a clearly shows that most Xe atoms were in the grain boundary region. This is because Xolotl provides a gas source term at grain boundaries only. This can be considered a limitation to this approach because the total free energy did not account for the intragranular gas content. Figure 4 shows the evolution of the total free energy as a function of burnup at both temperatures. The free energies were equivalent until approximately 20 MWd/kgU, where the free energy of the higher-temperature system started to increase faster than that of the lower-temperature system. Considering the results shown in Figure 2, this is a reasonable result. Note that at 950°C grain growth was thermally activated, which reduced the total free energy, whereas at 800°C, grain boundary mobility was limited.

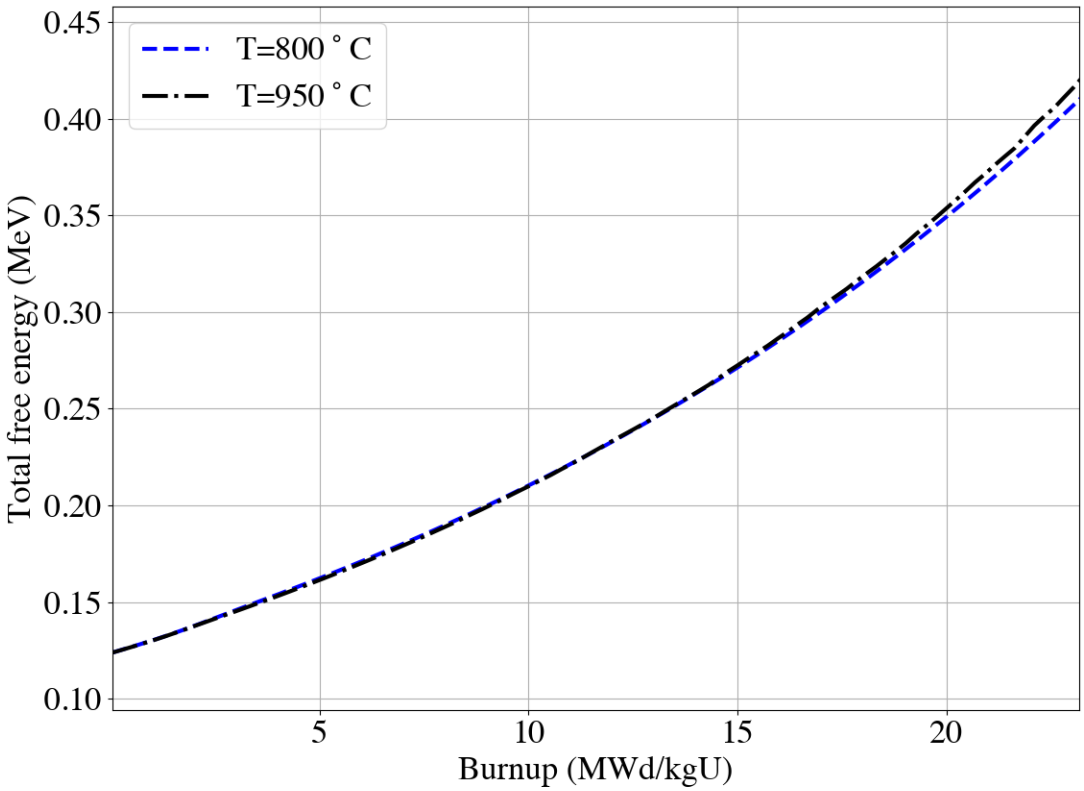

Figure 4. Evolution of the total free energy with burnup at T = 800°C and T = 950°C.

5. CONCLUSION

The development and improvement of nuclear fuel concepts for safer and more efficient reactor operation is crucial because of the increasing demand and need for nuclear power in the United States. Along with the extensive post irradiation examination (PIE) efforts to evaluate fuel performance factors such as fission gas release, fuel swelling, and cracking, advanced modeling and simulation tools play a major role in understanding the underlying physics and mechanisms of fuel performance. Accelerated fuel qualification enables more rapid assessment of fuel performance and microstructural evolution with burnup. MiniFuel irradiations [1] at the High Flux Isotope Reactor (HFIR) in Oak Ridge National Laboratory have been performed recently to gather PIE data on UO2 MiniFuel specimens.

Previous work modeled restructuring in the lower-temperature region of an LWR fuel pellet by combining a MARMOT phase field radiation damage model that tracks UO2 grain boundaries and fission gas bubbles and a nucleation algorithm. A physics-based model was developed to predict the onset of nucleation of smaller grains, thus simulating the restructuring reported in the literature [14, 15]. In continuation of this effort, the present work adds significant capabilities to our previous UO2 microstructural evolution model by accounting for the clustering and re-solution of fission gas atoms as well as the Monte Carlo simulation-based production rates of point defects and their reaction terms. Additionally, classical nucleation theory (CNT)–based model to evaluate the probability of intergranular fission gas bubble nucleation in the microstructure was included. These additional layers of complexity significantly improve the model's physics and enable the simulation of UO2 microstructures from the initial condition of the UO2 up to high burnup.

6. REFERENCES

[1] C. M. Petrie, J. R. Burns, A. M. Raftery, A. T. Nelson, and K. A. Terrani. Separate effects irradiation testing of miniature fuel specimens. *Journal of Nuclear Materials*, 526:151783, 2019.

[2] J.D. Hales, S.R. Novascone, B.W. Spencer, R.L. Williamson, G. Pastore, and D.M. Perez. Verification of the bison fuel performance code. *Annals of Nuclear Energy*, 71:81–90, 2014.

[3] Y. Zhang, D. Schwen, D. Andersson, M. Tonks, S. Novascone, and K. Ahemed. Introduction of the meso-scale fuel performance modeling code marmot. *Transactions of the American Nuclear Society*, 118:1340–1342, 2018.

[4] A. Cheniour, R. T. Sweet, A. T. Nelson, B. A. Wilson, and A. E. Shields. Sensitivity of UO_2 fuel performance to microstructural evolutions driven by dilute additives. *Nuclear Engineering and Design*, 410:112383, 2023.

[5] K. Lassmann, C. T. Walker, J. Van de Laar, and F. Lindström. Modelling the high burnup UO_2 structure in LWR fuel. *Journal of Nuclear Materials*, 226(1-2):1–8, 1995.

[6] L. K. Aagesen, D. Schwen, M. R. Tonks, and Y. Zhang. Phase-field modeling of fission gas bubble growth on grain boundaries and triple junctions in UO_2 nuclear fuel. *Computational Materials Science*, 161:35–45, 2019.

[7] D.-U. Kim, S. Blondel, D. E. Bernholdt, P. Roth, F. Kong, D. Andersson, M. R. Tonks, and B. D. Wirth. Modeling mesoscale fission gas behavior in UO_2 by directly coupling the phase field method to spatially resolved cluster dynamics. *Materials Theory*, 6(1):1–28, 2022.

[8] M. R. Tonks, A. Cheniour, and L. Aagesen. How to apply the phase field method to model radiation damage. *Computational Materials Science*, 147:353–362, 2018.

[9] M. G. Abdoelatef, F. Badry, D. Schwen, C. Permann, Y. Zhang, and K. Ahmed. Mesoscale modeling of high burn-up structure formation and evolution in UO_2. *Jom*, 71(12):4817–4828, 2019.

[10] L. Verma, L. Noirot, and P. Maugis. Modelling intra-granular bubble movement and fission gas release during post-irradiation annealing of uo2 using a meso-scale and spatialized approach. *Journal of Nuclear Materials*, 528:151874, 2020.

[11] L.-Q. Chen. Phase-field models for microstructure evolution. *Annual Review of Materials Research*, 32(1):113–140, 2002.

[12] L. K. Aagesen, S. Biswas, W. Jiang, D. Andersson, M. W. D. Cooper, and C. Matthews. Phase-field simulations of fission gas bubbles in high burnup uo2 during steady-state and loca transient conditions. *Journal of Nuclear Materials*, 557:153267, 2021.

[13] Y. Li, S. Hu, R. Montgomery, F. Gao, and X. Sun. Phase-field simulations of intragranular fission gas bubble evolution in uo2 under post-irradiation thermal annealing. *Nuclear Instruments and Methods in Physics Research Section B: Beam Interactions with Materials and Atoms*, 303:62–67, 2013.

[14] T. J. Gerczak, C. M. Parish, P. D. Edmondson, C. A. Baldwin, and K. A. Terrani. Restructuring in high burnup UO_2 studied using modern electron microscopy. *Journal of Nuclear Materials*, 509:245–259, 2018.

[15] K Nogita and K Une. Irradiation-induced recrystallization in high burnup UO_2 fuel. *Journal of Nuclear Materials*, 226(3):302–310, 1995.

[16] D. Schwen, S. Schunert, and A. Jokisaari. Evolution of microstructures in radiation fields using a coupled binary-collision monte carlo phase field approach. *Computational Materials Science*, 192:110321, 2021.

[17] A. Cheniour. *Study of U_3Si_2 fuel microstructure behavior under LWR conditions using the phase field method*. PhD thesis, University of Florida, 2020.

[18] C. J. Permann, D. R. Gaston, D. Andrš, R. W. Carlsen, F. Kong, A. D. Lindsay, J. M. Miller, J. W. Peterson, A. E. Slaughter, R. H. Stogner, and R. C. Martineau. MOOSE: Enabling massively parallel multiphysics simulation. *SoftwareX*, 11:100430, 2020.

[19] L. K. Aagesen, Y. Gao, D. Schwen, and K. Ahmed. Grand-potential-based phase-field model for multiple phases, grains, and chemical components. *Physical Review E*, 98(2):023309, 2018.

[20] M. Plapp. Unified derivation of phase-field models for alloy solidification from a grand-potential functional. *Physical Review E*, 84(3):031601, 2011.

[21] J. Rest and G. L. Hofman. Dynamics of irradiation-induced grain subdivision and swelling in U_3Si_2 and UO_2 fuels. *Journal of Nuclear materials*, 210(1-2):187–202, 1994.

[22] M. G. Marquez, A. M. Ougouag, and B. Petrovic. Model for radiation damage-induced grain subdivision and its influence in U_3Si_2 fuel swelling. *Annals of Nuclear Energy*, 145:105712, 2020.

[23] J. A. Turnbull, C. A. Friskney, J. R. Findlay, F. A. Johnson, and A. J. Walter. The diffusion coefficients of gaseous and volatile species during the irradiation of uranium dioxide. *Journal of Nuclear Materials*, 107(2-3):168–184, 1982.

[24] H. Matzke. Atomic transport properties in UO_2 and mixed oxides $(U, Pu)O_2$. *Journal of the Chemical Society, Faraday Transactions 2: Molecular and Chemical Physics*, 83(7):1121–1142, 1987.

[25] R. O. A. Hall, M. J. Mortimer, and D. A. Mortimer. Surface energy measurements on UO_2 – a critical review. *Journal of Nuclear Materials*, 148(3):237–256, 1987.

[26] C. J. Permann, M. R. Tonks, B. Fromm, and D. R. Gaston. Order parameter re-mapping algorithm for 3d phase field model of grain growth using fem. *Computational Materials Science*, 115:18–25, 2016.

[27] W. Wu, D. Montiel, J. E. Guyer, P. W. Voorhees, J. A. Warren, D. Wheeler, L. Gránásy, T. Pusztai, and O. G. Heinonen. Phase field benchmark problems for nucleation. *Computational Materials Science*, 193:110371, 2021.

[28] T. Takaki, T. Hirouchi, Y. Hisakuni, A. Yamanaka, and Y. Tomita. Multi-phase-field model to simulate microstructure evolutions during dynamic recrystallization. *Materials transactions*, 49(11):2559–2565, 2008.

[29] D. Xu and B. D. Wirth. Modeling spatially dependent kinetics of helium desorption in BCC iron following He ion implantation. *Journal of nuclear materials*, 403(1-3):184–190, 2010.

[30] S. Blondel, D. E. Bernholdt, K. D. Hammond, and B. D. Wirth. Continuum-scale modeling of helium bubble bursting under plasma-exposed tungsten surfaces. *Nuclear Fusion*, 58(12):126034, 2018.

[31] H. R. Faust. A model for fragment excitation and kinetic energy in nuclear fission. *The European Physical Journal A - Hadrons and Nuclei*, 14(4):459–468, Aug 2002.

[32] J. P. Crocombette, F. Jollet, L. Thien Nga, and T. Petit. Plane-wave pseudopotential study of point defects in uranium dioxide. *Physical Review B*, 64(10):104107, 2001.

[33] P. V. Nerikar, X.-Y. Liu, B. P. Uberuaga, C. R. Stanek, S. R. Phillpot, and S. B. Sinnott. Thermodynamics of fission products in $UO_2 \pm x$. *Journal of Physics: Condensed Matter*, 21(43):435602, 2009.

[34] M. Idiri, T. Le Bihan, S. Heathman, and J. Rebizant. Behavior of actinide dioxides under pressure: UO_2 and ThO_2. *Physical Review B*, 70(1):014113, 2004.

[35] J. B. Ainscough, B. W. Oldfield, and J. O. Ware. Isothermal grain growth kinetics in sintered UO_2 pellets. *Journal of Nuclear Materials*, 49(2):117–128, 1973.

[36] P. V. Nerikar, K. Rudman, T. G. Desai, D. Byler, C. Unal, K. J. McClellan, S. R. Phillpot, S. B. Sinnott, P. Peralta, B. P Uberuaga, et al. Grain boundaries in uranium dioxide: scanning electron microscopy experiments and atomistic simulations. *Journal of the American Ceramic Society*, 94(6):1893–1900, 2011.